A 4-D FMCW LiDAR With Ultra-High Velocity Sensitivity

Yu-Xiang Lin, Zohauddin Ahmad, Sung-Yi Ou, Wei-Chih Su ⬤, Yan-Chieh Chang, Naseem ⬤, Jye-Hong Chen, Yung-Jr Hung ⬤, *Member, IEEE*, You-Chia Chang ⬤, Chia-Chien Wei ⬤, *Member, IEEE*, Tzyy-Sheng Horng ⬤, *Fellow, IEEE*, and Jin-Wei Shi ⬤, *Senior Member, IEEE*

Abstract—This work presents a novel scheme for a 4-dimensional (D) frequency modulated continuous wave (FMCW) LiDAR, which demonstrates an unprecedentedly high velocity sensitivity. This is achieved by utilizing the driving waveform to minimize the phase noise originating from the distributed feedback (DFB) laser during the wavelength sweeping process on the transmitting side, while on the receiving end, we use a combination of a self-injection-locked oscillator (SILO) and an avalanche photodiode (APD) with a cascaded multiplication layer, to ensure excellent responsivity and saturation current performance. Comparison is made with a reference LiDAR system comprised of the traditional radio-frequency (RF) oscillator with a p-i-n PD at the receiving-end. The results show that our SILO + APD design provides much better quality 4-D images of slow-moving objects (5 μm/sec) and state-of-the-art velocity sensitivity. This can be attributed to a reduction in the phase noise of the down-converted baseband signals, which is beneficial to the resolution of a small Doppler frequency shift. Furthermore, the incorporation of a high-performance APD also improves the contrast ratio between the object and the background pixels. These improvements offer new possibilities for the development of the next generation of 4-D FMCW LiDARs capable of simultaneously providing the absolute 3-D geometric size and small vibration information.

Index Terms—Avalanche photodiodes (APDs), image detection systems.

Yu-Xiang Lin and Sung-Yi Ou are with the Department of Electrical Engineering, National Central University, Taoyuan 320, Taiwan, and also with the Department of Photonics, National Sun Yat-Sen University, Kaohsiung 80424, Taiwan (e-mail: yom12347@gmail.com; syoung07890@gmail.com).

Zohauddin Ahmad, Yan-Chieh Chang, Naseem, and Jin-Wei Shi are with the Department of Electrical Engineering, National Central University, Taoyuan 320, Taiwan (e-mail: zohauddin145991@st.jmi.ac.in; cyds60408@gmail.com; naseemever3@gmail.com; jwshi@ee.ncu.edu.tw).

Wei-Chih Su and Tzyy-Sheng Horng are with the Department of Electrical Engineering, National Sun Yat-Sen University, Kaohsiung 80424, Taiwan (e-mail: whitewager@gmail.com; jason@ee.nsysu.edu.tw).

Jye-Hong Chen and You-Chia Chang are with the Department of Photonics and Institute of Electro-Optical Engineering, National Yang Ming Chiao Tung University, Hsinchu 30010, Taiwan (e-mail: jchen@nycu.edu.tw; youchia@nycu.edu.tw).

Yung-Jr Hung and Chia-Chien Wei are with the Department of Photonics, National Sun Yat-Sen University, Kaohsiung 80424, Taiwan (e-mail: yungjr@mail.nsysu.edu.tw; ccwei@mail.nsysu.edu.tw).

Color versions of one or more figures in this article are available at https://doi.org/10.1109/JLT.2023.3292139.

Digital Object Identifier 10.1109/JLT.2023.3292139

I. INTRODUCTION

FREQUENCY modulated continuous wave (FMCW) radars have found applications in various industries, for example, for velocity measurement in automotive and military sensors [1], [2], for hand gesture recognition (HGR) [3], and for non-contact vital-sign monitoring (VSM) in medical applications [4], [5]. This technique has several unique advantages over other radar technologies, being able to obtain instantaneous velocity information for (multiple-) objects and the elimination of the blind time during operation. However, it is desirable to improve the velocity sensitivity detection capability of FMCW radar to meet the requirements for HGR and VSM applications.

Several strategies have been demonstrated to minimize the influence of the phase noise on small Doppler frequency shifts (<1Hz) in the received radio-frequency (RF) signal, such as by the incorporation of an RF self-injection-locked oscillator (SILO) into the design [5], [6] or improvement of the signal processing algorithms [4].

However, obtaining real-time 4-D (3D + velocity) images with an FMCW radar with a compact antenna size remains a challenge. One of the most effective steps towards attaining such a goal is development of the FMCW LiDAR architecture, which merges the FMCW radar with additional electrical-to-optical (EO) and optical-to-electrical (OE) conversion modules [7], [8], [9], [10], [11], [12], [13]. 4-D images have been obtained at the optical wavelength of 1.55 μm using a miniaturized FMCW LiDAR module containing compact internal optics [14]. These LiDAR images also usually exhibit much better angular resolution in both azimuth and elevation than those of FMCW radar [7]. In addition, an improvement in the high velocity sensitivity can also be expected when the central frequency is boosted from the RF to the optical wave range. Although the commercially available laser vibrometers have demonstrated ultra-high velocity sensitivity (∼nm/sec) [15] it is not as simple to obtain a 3-D profile with absolute distance information from the interference signal as it is for a static laser.

In order to successfully realize a 4-D FMCW LiDAR design, it is essential for a wavelength sweeping laser to serve as a light source. Recently, there has been an increase in demand for 4-D FMCW LiDARs with a velocity sensitivity as high as that of the vibrometer, which are capable of simultaneously measuring the physical parameters and dynamic fine displacement of civil structures in real time [16].

Unfortunately, wavelength sweeping lasers tend to suffer from much larger phase noise and nonlinearity than do static lasers [17], which can seriously limit their capability to resolve the small Doppler frequency shifts required for high velocity sensitivity performance. The self-injection-locked (SIL) technique [18] has been adapted for semiconductor laser applications and the devices thus designed have demonstrated state-of-the-art static and instantaneous optical linewidths down to the Hz level [18], [19], [20]. However, in addition to phase noise from the laser transmitter side, phase noise from the electrical LO source during the frequency down-conversion process on the receiver-end of the LiDAR is also an issue.

In this work, we combine a SILO RF oscillator [5], [6] with our home-made avalanche photodiode (APD), which has already demonstrated excellent saturation current and responsivity performance [21], [22], to reduce phase and amplitude noise on the receiver-side of the FMCW LiDAR. As compared to the traditional architecture with a p-i-n photodiode (PD) at the receiver-end, our unique APD structure shows a high responsivity, large gain-bandwidth product, and low excess noise under a moderate (~mW) optical LO pumping power, which can further increase the optical power budget and velocity sensitivity of the FMCW LiDAR system [22]. This breakthrough in the receiver-end design has allowed us to successfully capture 4-D images with an unprecedented high velocity sensitivity (~5 μm/sec). In contrast to using a SIL laser, which relies on a high-Q optical cavity in the optical domain [18], [19], [20], it is not necessary to include a high-Q RF resonator to suppress phase noise in the RF SILO design. It can thus be implemented as an integrated circuit (IC) [23] allowing for a compact low-cost package. In contrast to the reference system which relies upon the traditional p-i-n PD and heterodyne RF receivers (rather than the SILO), our LiDAR system can construct much better quality 4-D images of a slow-moving (~ 5 μm/sec) object, because of the enhancement of the contrast ratio between the object and background signals in each pixel. Even when the object is moving at such a low speed, our new scheme can greatly reduce (by about 50%) the mean velocity measurement error. The improvement in the baseband spectra demonstrated by our FMCW LiDAR system opens up new possibilities for the development of a new generation of 4-D LiDARs capable of providing real-time 4-D images with a velocity sensitivity as high as that of the state-of-the-art laser vibrometers.

II. SYSTEM SETUP

Fig. 1 shows the setup of our FMCW LiDAR system. In order to attain the highest velocity sensitivity, the receiver-end in the LiDAR must be able to discriminate a small Doppler frequency shift (f_D), down to a level of several Hz. This will be discussed in more detail later. In addition, for real-time applications, it is highly desirable to select a small baseband bandwidth (tens of kHz), to avoid the necessity of using costly high-speed signal processing ICs in the receiver-end. However, laser flicker noise becomes a serious issue under low-frequency operation. A heterodyne scheme is adopted to overcome this problem in our LiDAR system [21], where the frequency of the FMCW laser for
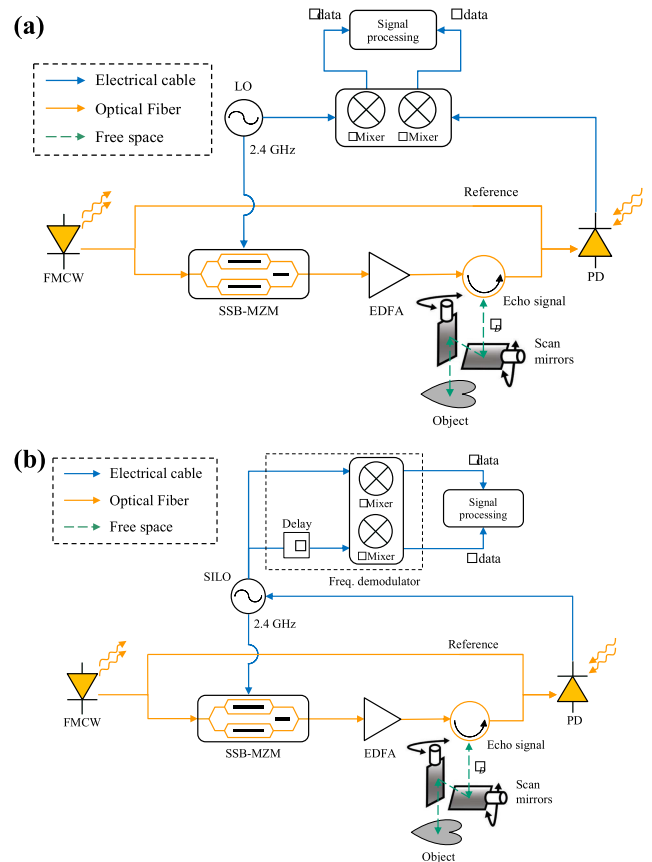

Fig. 1. The setups for the (a) conventional heterodyne and (b) self-injection schemes.

sensing an object is up-converted by an additional 2.4 GHz (i.e., the intermediate frequency (IF, f_{IF}) using a single-sideband (SSB) Mach-Zehnder modulator (MZM), which is driven by a local oscillator (LO), to avoid the flicker noise.

A comparison is made between the two different types of designs with photodetectors in the receiver-end. Our home-made avalanche photodiode (APD) with cascaded multiplication layers [21] offers superior responsivity and saturation current performance over that of the p-i-n PDs for FMCW LiDAR applications [21]. The responsivity performance can be further enhanced over that reported in our previous work [21], [22] by replacing the APD with its top-illuminated structure, with a new flip-chip bonding package, in which the topside contact metal can serve as an optical mirror to fold the absorption path of optical signals launched from the substrate side. The dynamic and static measurement results obtained with this novel device will be discussed below.

Comparison is made with a high-performance, commercially available p-i-n PD based Rx (Thorlabs, RXM42AF) device, which is composed of a high-speed p-i-n PD integrated with a trans-impedance amplifier (TIA). After passing through the PD or APD, the signal is down converted to the baseband using the LO and a quadrature mixer, as shown in Fig. 1(a). Improved 4-D image quality can be expected with the SILO-assisted LiDAR system, because self-injection locking makes it possible to

provide the gain in the signal-to-noise (S/N) ratio [5], [6], especially for a weak low-frequency signal. To realize RF self-injection in the receiver-end, the beating signal between the echo and the reference light is injected into the LO to modulate the output frequency. In other words, the LO operates as a SILO, as shown in Fig. 1(b). A frequency demodulator composed of a mixer and a delay line is then used to extract the Doppler frequency shift from the LO output signal. The working principles of our SILO are discussed below.

The IF beating signal in the heterodyne receiver can be represented by

$$S_{IF}(t) = A_{IF} \cos\left(\omega_{IF}t + \phi_{IF}(t)\right), \tag{1}$$

where ω_{IF}, A_{IF}, and ϕ_{IF} are the angular frequency, amplitude, and phase of the IF beating signal, respectively. It is important to note that ϕ_{IF} incorporates the phase information of both the beating frequency and the Doppler frequency shift. In the self-injection scheme, when the SILO is injected with the IF beating signal, the output signal undergoes frequency modulation, which can be described by

$$\Delta\omega_{SILO}(t) = \omega_{LR} \sin\left(\phi_{IF}(t)\right). \tag{2}$$

Here, ω_{LR} represents the locking range of the SILO which is given by

$$\omega_{LR} = \frac{\omega_{SILO}A_{IF}}{2Q_{\text{SILO}}A_{SILO}}. \tag{3}$$

In (3), ω_{SILO}, Q_{SILO}, and A_{SILO} correspond to the angular frequency, tank quality factor, and oscillation amplitude of the SILO, respectively. The output baseband signal obtained after employing frequency demodulation in the SILO, is as follows:

$$B_{SI}(t) = \Delta\omega_{SILO}(t)\tau_d, \tag{4}$$

where τ_d denotes the time delay of the delay line used in the frequency demodulator. In contrast, the conventional heterodyne scheme produces the following baseband signal

$$B_{CH}(t) = A_{IF}e^{j\phi_{IF}(t)}. \tag{5}$$

Comparing (4) with (5), we can derive the amplitude gain achieved through the self-injection scheme:

$$G_B = \frac{\omega_{SILO}\tau_d}{2Q_{SILO}A_{SILO}}. \tag{6}$$

It is worth noting that, by substituting the relevant design parameters into (6), G_B exceeds 30 dB. Such a large internal gain in the SILO leads to a much better 4-D image quality than that of the conventional heterodyne receiver as will be discussed later.

To illuminate the object, a fiber collimator is used to generate a free-space beam, and a pair of galvo scan mirrors (Thorlabs, GVSM002-US) is used to scan the beam direction in two dimensions, as shown in Fig. 1(a) and (b). At the output of the fiber collimator, the beam has a Gaussian diameter of 0.87 mm and a divergence angle of 0.129°. The scanning mirrors allow beam scanning with a field-of-view of ±12.5° and a repeatability of 15 μrad. The light reflected by the object is received by the same fiber collimator, and a circulator is used to redirect the reflected light toward the photoreceiver.
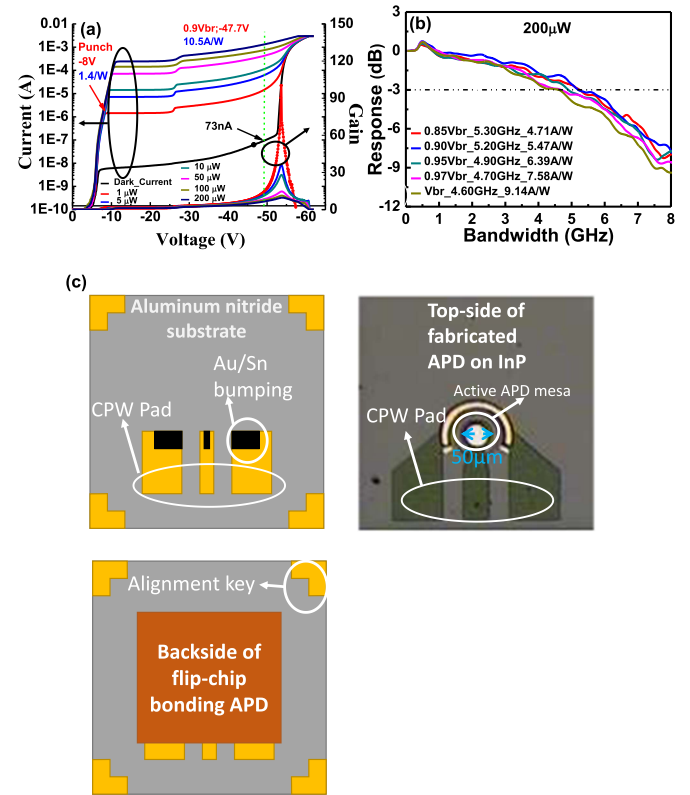

Fig. 2. (a) I-V characteristics of the demonstrated APD under different input optical powers (b) bias-dependent O-E frequency responses measured under a moderate optical pumping power (200 μW) (c) top-views of the demonstrated APDs before and after flip-chip bonding.

III. RESULTS

Fig. 2(a) shows the bias dependent photocurrent, dark current, and multiplication gain of the demonstrated APD. Comparison of the reference top-illuminated APD, which has the same epi-layer structure (triple M-layer design [21]) as the APD described in this work shows a significant improvement in the responsivity (7.7 vs. 10.5 A/W at 0.9 V_{br}) while maintaining a close 3-dB bandwidth value. Furthermore, under 0.9 V_{br}, the gain is almost invariant when the launched optical power ranges between 0.05 to 0.2 mW. This is close to the optimum optical LO pumping power (~0.2 mW) level required to obtain the highest S/N ratio. In contrast to the traditional APD, for weak light applications, the aim of our APD is to produce high-responsivity and high-speed performance under a moderate optical LO pumping power, which is suitable for FMCW LiDAR applications. Fig. 2(b) shows the bias dependent optical-to-electrical (O-E) frequency responses measured under the optimal optical power (0.2 mW). As can be seen, the measured 3-dB optical-to-electrical (O-E) bandwidth can reach 5.2 GHz with a high-responsivity (5.5 A/W at 0.9 V_{br}) and the bandwidth number remains nearly constant over different bias voltages (0.85 to 1 V_{br}). Both these bias/power insensitive characteristics are indicative of the high-linearity performance of our APD, which is a key parameter for FMCW LiDAR applications. For more details about device performance, the interested reader can refer to our previous work [21]. The layout of metal pads on the aluminum nitride (AlN)

TABLE I
BENCHMARK APD PERFORMANCE IN LiDAR APPLICATIONS

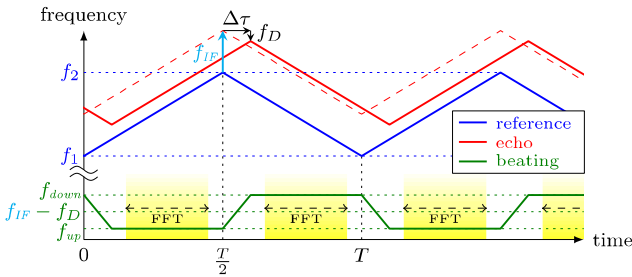| Parameters	Condition	Excelitas (C30662)	Hamamatsu (G14858-0020AB)	GaAsSb/ AlGaAsSb	Our topside APD	Unit
Active diameter	-	0.2	0.2	0.2	0.2	mm
Gain	Maxima	20	30	278	440	-
Responsivity	M=1	-	0.8	0.17	1.0	A/W
Bandwidth	M=10	0.85	0.9	0.7 at M=25	1.4 at M=25	GHz
Breakdown voltage	V_{br}	50	65	70	45	V
Dark current	$0.95V_{br}$	45	20	480	300	nA
Ref no.	-	24	25	26	21	-

Fig. 3. Schematic representation of frequency versus time in FMCW mode.

carrier substrate is illustrated in Fig. 2(c), along with top-views of the fabricated APD with a 50 μm diameter active optical window on the InP substrate, and the flip-chip bonding package. Here, the co-planar waveguide (CPW) structure is adopted on both the active APD and passive AlN carrier side during the flip-chip bonding process.

Comparison is made between the performance of our previously fabricated 200 μm active diameter top-illuminated APD [21] and the commercially available APDs [24], [25], [26]. As can be seen in Table I, the multiple M-layer APD outperforms the APDs obtained from different suppliers [24], [25], [26] with respect to gain, responsivity, and smaller V_{br}, while maintaining a better O-E bandwidth. These results show the immense potential of our APD design for utilization in LiDAR systems.

To enable simultaneous detection of the distance and velocity of an object, the FMCW is modulated by a periodic triangular waveform signal. Ideally, the instantaneous frequency of the FMCW laser will vary linearly from f_1 to f_2 and back again during the intervals of rising (up-chirp) and falling (down-chirp) frequency, as shown in the schematic representation in Fig. 3. Part of the FMCW laser output is directly used as the reference light, while the other part is modulated to produce the frequency change of f_{IF} before being directed to the object. As shown in Fig. 3, the difference in the frequencies of the reference and echo lights is not only the IF, because of the relative delay and the Doppler shift caused by the objects being tested. Thus, the

frequencies of the beating signals for the up- and down-chirp intervals are different and are able to reveal information about the distance and velocity of the objects. Specifically, the frequencies of the RF beating signal at the two intervals are [27]

$$f_{up} = f_{IF} - \frac{2(f_2 - f_1)}{T}\Delta\tau - f_D,$$

$$f_{down} = f_{IF} + \frac{2(f_2 - f_1)}{T}\Delta\tau - f_D, \tag{7}$$

where T denotes the period of the triangular modulation, and $\Delta\tau$ is the time difference between when the light echo and the reference light arrive at the receiver. In addition to the intrinsic time difference $\Delta\tau_0$ caused by some fixed components, the relative distance L of the object being tested will linearly affect $\Delta\tau$. Thus,

$$\Delta\tau = \Delta\tau_0 + \frac{2L}{c}, \tag{8}$$

where c is the speed of light. Assuming that the laser frequency f_c is much greater than the sweep bandwidth $f_2 - f_1$, the Doppler shift is a linear function of the velocity v of the object,

$$f_D = \frac{2f_c}{c} v. \tag{9}$$

However, if the laser frequency sweep is not perfectly triangular, the beating signals for the up- and down-chirp intervals will not have constant frequencies, making it difficult to determine the values of f_{up}, f_{down} and $\Delta\tau$. The driving waveform must be pre-distorted for optimal linearity performance. Fig. 4 shows the linearization process for the FMCW laser [28]. The difference between the measured and the desired laser frequency sweep is used to iteratively update the driving signal.

The laser frequency, as shown in Fig. 4, is measured by the heterodyne scheme; it is revealed by the beating signal of the FMCW laser and stable narrow-linewidth tunable laser (HP 8167B). The function of the tunable laser is to convert the frequency of the FMCW laser down to within the bandwidth of the optical receiver. Thus, the frequency of the tunable laser
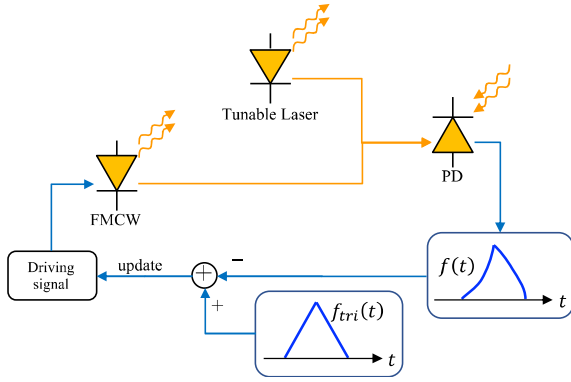
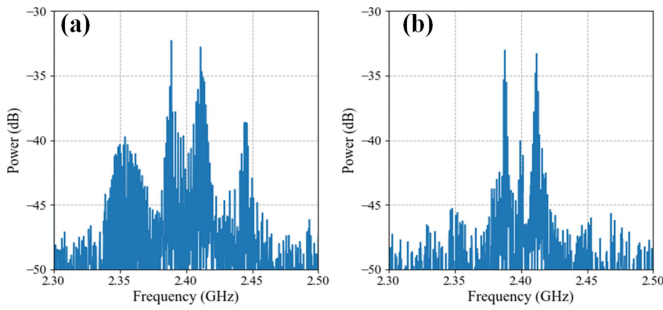Fig. 4.   Laser frequency sweep linearization process.

Fig. 5.   Electrical spectra detected (a) before and (b) after the linearization of the laser frequency sweep.

f_0 is set to lower than but close to f_1, such that the frequency range of the beating signal (i.e., $f_1 - f_0$ to $f_2 - f_0$) falls within the spectrum of the same side, making detection by a single-PD feasible.

In the experiments, a 1-kHz driving signal was generated by an arbitrary waveform generator (Keysight, M8190A). Starting with the ideal triangular driving signal, only five iterations were required to obtain the pre-distorted driving signal needed to reach the best laser frequency sweep linearity, with a sweep bandwidth B (i.e., $f_2 - f_1$) of 13 GHz, leading to a range resolution of $c/(2B) = 1.15$ cm [9]. Fig. 5 shows the measured spectra of the beating signal between the light echo and reference light obtained before and after linearization of the laser frequency sweep for a static object. There are two spectral peaks, at frequencies of f_{up} and f_{down}, for which the 10-dB spectral widths are 16 and 18 kHz (as shown in Fig. 5(a)) and 9 and 11 kHz (in Fig. 5(b)), respectively. The significant reduction in the spectral widths indicates that the linearization of the laser frequency sweep has been successful. The linearization also eliminates the undesired harmonics at 2.35 and 2.45 GHz, as shown in Fig. 5(a), reducing the possibility of misidentification of f_{up} and f_{down}.

With the exception of the sweeping laser, the APD operating conditions, including the bias voltage and optical LO pumping (i.e., the reference light) power, were optimized to obtain the best spectral identification for each pixel. Fig. 6(a)–(c) show the bias-dependent baseband spectra obtained with the self-injection scheme illustrated in Fig. 1(b), under a fixed optical LO of −5
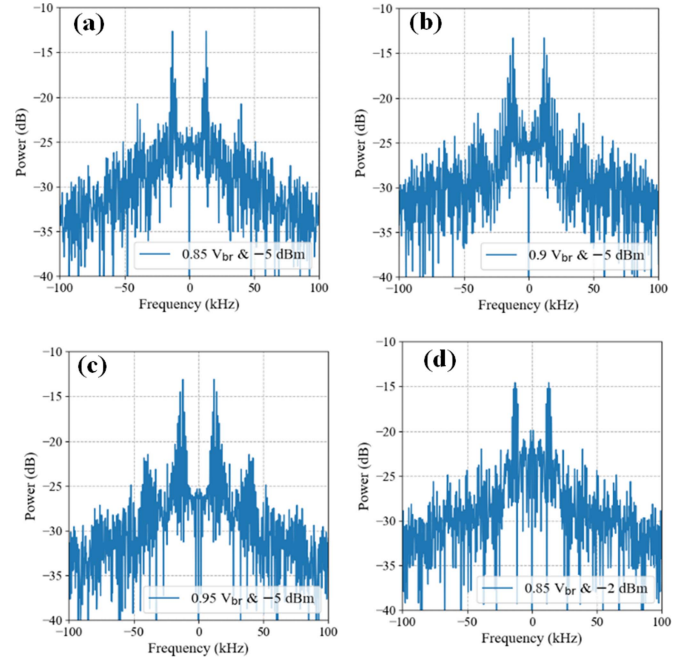

Fig. 6.   Baseband spectra measured at a fixed LO power of −5 dBm and different reverse bias voltages (a) 0.85 V_{br} (b) 0.9 V_{br} (c) 0.95 V_{br}. (d) Baseband spectra obtained under an optimized 0.85 V_{br} but at a higher LO power of −2 dBm.
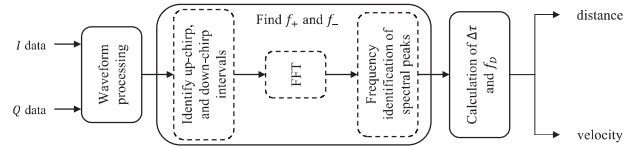

Fig. 7.   Signal processing for distance and velocity sensing.

dBm. As can be seen, the 10-dB spectral widths are 5.4, 19, and 11 kHz; the narrowest width is obtained at 0.85 V_{br}. The optical LO power-dependent baseband spectra obtained under optimal 0.85 V_{br} APD operation are depicted in Fig. 6(a) and (d). As can be seen, the spectral widths are about the same, and the LO power dependency is not very significant. Thus, the lower LO power (−5 dBm) is chosen for application during measurement to increase the power budget for ranging.

Fig. 7 depicts the flow of the off-line signal process applied to obtain the distance and velocity. First, the received in-phase and quadrature data (I and Q) are recorded by a real-time oscilloscope (Keysight, DSO81204A) using a sample rate of 250 kSample/s and processed into a single data stream. The data stream required for the self-injection scheme is derived from the phase difference between the output of the SILO and the delayed version, i.e., $\tan^{-1}(Q/I)$. The conventional (heterodyne) scheme simply requires the complex baseband signal, i.e., $I + jQ$.

Theoretically speaking, the spectra of the data streams should reveal the values of f_{up} and f_{down}. However, if the fast-Fourier transform (FFT) is applied to a processed stream, for which the time length is longer than the modulation period T, the corresponding spectrum will simultaneously contain multiple
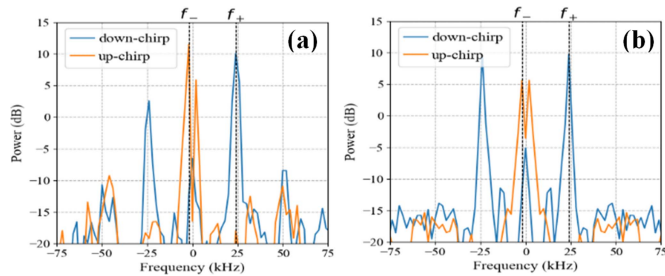
Fig. 8. Signal processing for distance and velocity sensing. The spectra obtained during the up- and down-chirp intervals with the (a) conventional and (b) self-injection schemes.

Fig. 9. Placement of targets (I, ♡, and U) at a specified distance for testing.

frequency components. Specifically,, two spectral peaks can be observed in the negative and positive spectra at frequencies of $f_- = f_{up} - f_{IF}$ and $f_+ = f_{down} - f_{IF}$ with the conventional scheme. On the other hand, since $\tan^{-1}(Q/I)$ is inherently a real value, in the self-injection scheme, the two spectral peaks will appear together on each side, i.e., at $\pm|f_-|$ and $\pm|f_+|$. In both cases, the existence of multiple spectral components increases the difficulty of obtaining the desired spectral information. To clearly identify the frequency differences between the echo light and the reference light during the up- and down-chirp intervals, i.e., f_- and f_+ respectively, the streams during the two intervals are processed separately. The separation of the spectra allows for better identification of f_- and f_+. For example, look at the spectra obtained when the velocity of the object being tested is set to 10 mm/s. The spectra during the up- and down-chirp intervals are plotted in Fig. 8. The FFT interval is shorter, as depicted in Fig. 3. The single harmonic observed in each case indicates the successful elimination of multiple spectral components from the spectra. Using a short FFT interval makes identification of the spectral information much easier. As can be seen in Fig. 8(a), the two spectra are asymmetric and have spectral peaks on different sides. In contrast, the two spectra in Fig. 8(b) are symmetric. Therefore, the process for finding f_- and f_+ includes identification of the up- and down-chirp intervals from the synchronized data streams. The application of the FFT to each interval aids in frequency identification of the spectral peaks. After finding f_- and f_+, the last step, as illustrated in Fig. 7, is to calculate the distance and velocity using (7)–(9).

The capability of the system to simultaneously sense the distance and the velocity was tested using I, ♡, and U-shaped targets, which were made from Styrofoam wrapped in retrore-flective tape, as shown in Fig. 9. The ♡-shaped object was placed on a motorized linear stage which moved at a given speed, while the I and U-shaped targets remained static. The ♡-shaped object was moving during the measurement process, but the relative distances to the I, ♡, and U targets were different, 2, 7, and 12 cm, respectively. Note that the azimuth and elevation for 4D measurement were obtained by 40 by 40 pixel scanning in this work.

Fig. 10 shows the measured images of distance and motion obtained using the p-i-n PD; the ♡-shaped target was moving at 10 mm/s. A side-by-side visual comparison reveals the similarity

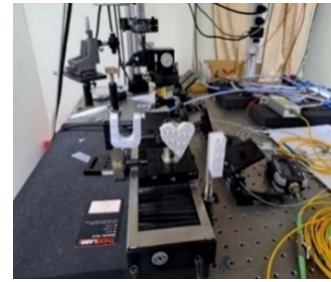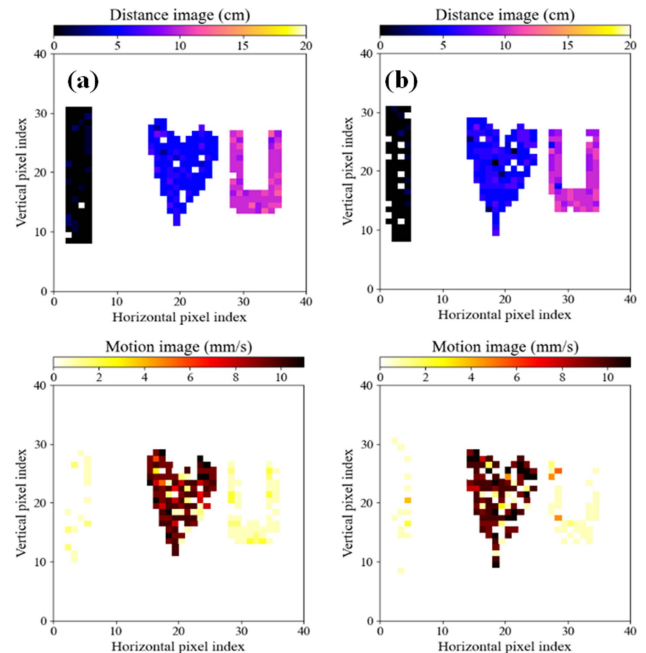Fig. 10. Images of distance and motion obtained using the FMCW mode with the (a) conventional and (b) self-injection schemes when the velocity of the ♡ is 10 mm/s.

in performance between the two schemes. Specifically, the average measurement errors for distance and velocity are about 0.4 cm and 2 mm/s, respectively, for both schemes. The relatively small error values mean that it is possible to differentiate the distances and velocities for the three objects. The results confirm that the distances and velocities can be successfully obtained with either scheme. Note that some image pixels do not appear because they have been mistakenly identified as part of the background, probably because of the less than ideal reflection. In the experiments, when the frequency of the spectral peak exceeded the range of the settings, it was regarded as a part of the background. Specifically, the set range is 3 times the maximum desired frequency, determined for the farthest object, in this case, the U-shaped target.

A lower speed (e.g., ≤1 mm/s) is required to test the difference in the ability to sense the motion between the two schemes. Fig. 11 shows the motion images measured at 1 mm/s. The visual results show the speeds of the static objects (I and U-shaped objects) and the moving ♡-shaped object to be similar; the average measurement errors for the static and moving objects
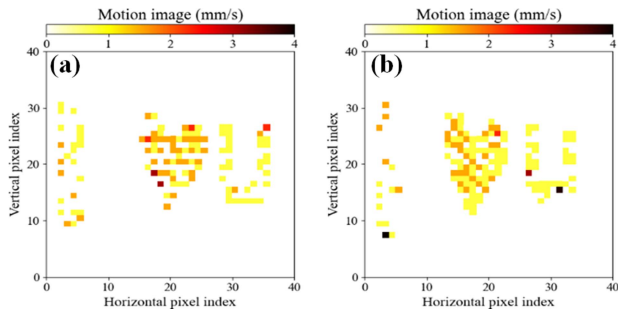
Fig. 11. Measured images of motion at 1 mm/sec obtained using the FMCW mode with the (a) conventional and (b) self-injection schemes.
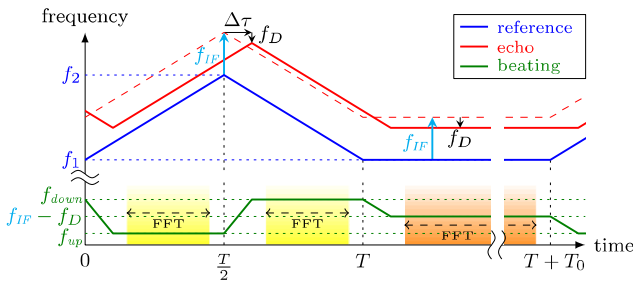

Fig. 12. Schematic plot of frequency versus time in the hybrid FMCW mode.

Fig. 13. Measured images of motion at 1 mm/sec obtained using the hybrid FMCW mode with the (a) conventional and (b) self-injection schemes.

obtained using the conventional (self-injection) schemes are 0.9 (0.75) and 1.2 (0.73) mm/s, respectively. The inaccuracy of the results seems to suggest that neither scheme is feasible for sensing an object at such a low speed. In fact, the limitation for sensing an object at a low speed is the length of the FFT interval. Here the length of the FFT interval is $T/2 = 500 \ \mu s$, giving a spectral resolution of 2 kHz; the Doppler frequency is only 1.3 kHz when the speed is 1 mm/s. Therefore, we suggest using the hybrid FMCW mode for the 4D measurement detection of objects moving at extremely low speeds.

The hybrid FMCW mode, see Fig. 12, is designed to generate an extra duration of constant frequency after several triangular frequency sweeps. The triangular frequency sweeps are still used to measure distance, but the velocity is determined by the constant-frequency duration, in which the frequency of the beating signal is determined by the speed of the object, regardless of the distance. When a high FFT resolution is needed for the analysis of a small f_D, the length of the constant-frequency duration T_0 can be increased without affecting the distance sensing while using triangular frequency sweeps. Therefore, as depicted in Fig. 7, in the hybrid FMCW mode, only the distance need be calculated during signal processing, the Doppler shift and velocity are obtained by identification of the constant-frequency interval, application of the FFT, and frequency identification of the spectral peak.

The hybrid FMCW mode is applied, with $T_0 = 0.1$ (or 1) sec, to achieve an FFT resolution of 10 (or 1) Hz during measurement, with speeds of ≥ 0.1 (or < 0.1) mm/s. Note that for motion sensing at 0.1 mm/s it is necessary to be able to detect a Doppler frequency of 130 Hz during the measurement process.
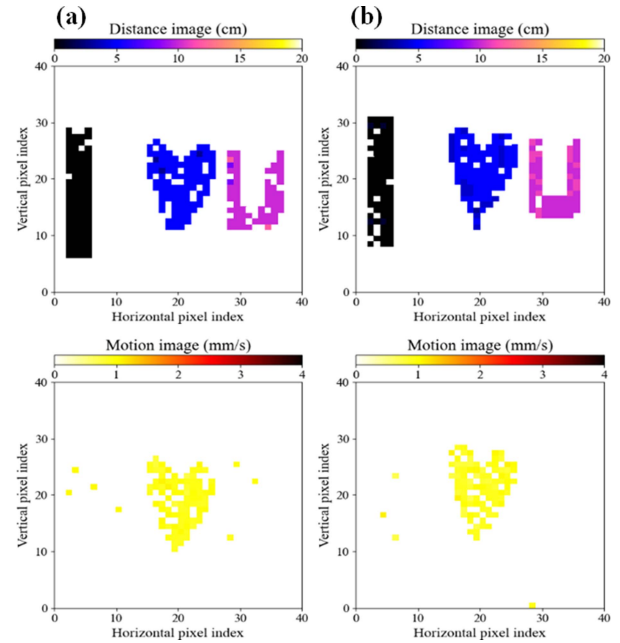
Fig. 13(a) and (b) show the measured images of distance and motion obtained using the conventional and self-injection schemes, respectively, with the hybrid driving waveform and the velocity of the $\heartsuit$ set to 1 mm/s. Since we still rely upon the same triangular frequency sweep for detection of distance in the hybrid mode, the images of distance are similar, in contrast to those obtained with the original FMCW mode, as shown in Fig. 11. In fact, the mean distance measurement errors in Figs. 11 and 13 are all about 0.4 cm, so that we can properly differentiate the distances of the symbols in the setup, regardless of which modulation mode and detection schemes are adopted. However, a comparison of the images in Figs. 11, and 13(a) and (b), with measurement errors of 0.29 and 0.28 mm/s, respectively, demonstrates a significant improvement in motion sensing under constant-frequency operation and a longer measurement interval in the hybrid FMCW mode. The better FFT resolution enables better measurement of lower speeds and improved sensitivity, for both the conventional and self-injection schemes; see Fig. 13. It is worth noting that the limited FFT resolution in the FMCW mode also results in a misjudgment in the motion sensing of some pixels in the letters I and U, as can be seen in Figs. 10 and 11; this is not the case in the hybrid FMCW mode.

To examine and compare the abilities of the two schemes for detection at a very low speed, the $\heartsuit$ symbol is set to move at only 0.01 mm/s. The images of motion are shown in Fig. 14. There are obviously more measurement errors in the images obtained using the conventional scheme than with the self-injection scheme. In particular, the conventional scheme shows few pixels with correct measurements, leading to an average measurement error of up to 0.009 mm/s. In contrast, with the self-injection scheme, measurement errors are relatively low in most pixels, with an
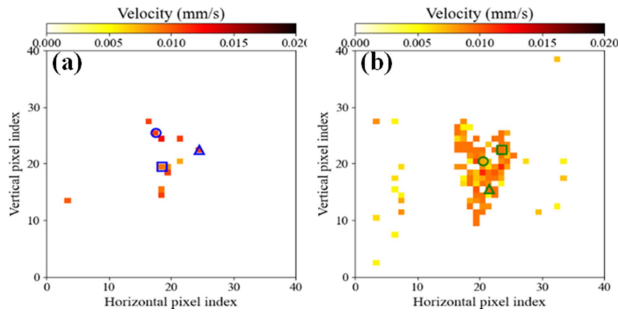
Fig. 14. Measured images of motion at 0.01 mm/s obtained using the hybrid FMCW mode with the (a) conventional and (b) self-injection schemes.
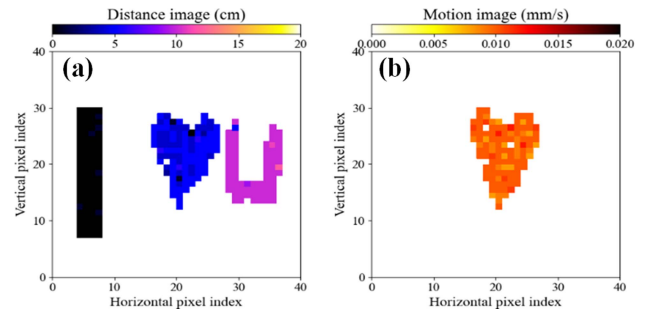

Fig. 16. Measured (a) 3-D location and (b) velocity images at a speed of 0.01 mm/sec obtained using the hybrid FMCW mode, self-injection scheme, and APD.
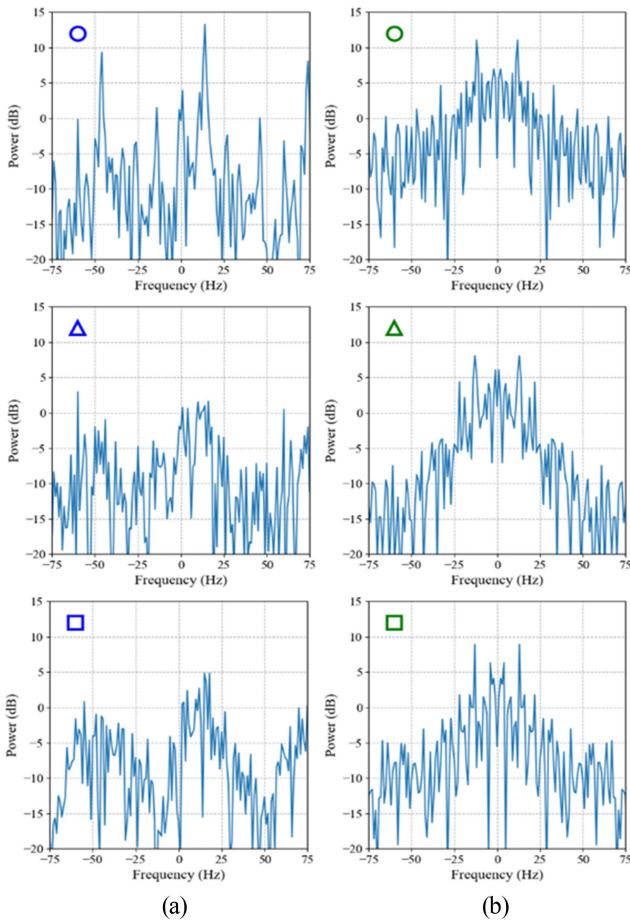

Fig. 15. The measured spectra in the constant-frequency intervals at a velocity of 0.01 mm/s using the (a) conventional and (b) self-injection schemes.

average error is 0.0038 mm/s. This result indicates the much better measurement accuracy of the self-injection scheme. When the speed of movement decreases further, the benefit becomes more pronounced on the receiver side.

For a more detailed comparison of the differences between the conventional and self-injection schemes, the spectra of some pixels selected from Fig. 14 are plotted in Fig. 15. The spectra in the 1st to the 3rd rows in Fig. 15 correspond to the pixels marked with the symbols ∘, □, and ▷, respectively, in Fig. 14. The frequency of the spectral peak indicates the Doppler shift. As shown in Fig. 15(b), clearer spectra can be obtained with the self-injection

scheme, which indicates that it is capable of achieving better velocity resolution, compared to the conventional scheme; see Fig. 15(a). The spectra obtained with the conventional scheme show more and wider spectral peaks, leading to an increased possibility of measurement error. In contrast, all the spectra in Fig. 15(b) are all relatively narrow. For instance, look at the 3rd row in Fig. 15. Using the conventional scheme, the power difference between the two spectral peaks is only ∼0.2 dB but for the self-injection scheme, the power difference is more than 2.7 dB.

The sensitivity to velocity can be further improved by replacing the p-i-n PD with our novel APD, thereby reducing the phase and amplitude noise in the detected signals. Fig. 16 plots the 4-D images measured at 0.01 mm/sec using the APD; the testing conditions are the same as in Fig. 14(b). The APD decreases the average error to 0.0033 mm/s; see Fig. 16(b). A comparison of the differences between the average error in Fig. 14(b) and (b) indicates that even better performance is obtained with the APD at a lower speed (0.01 mm/s) than is possible with the p-i-n PD.

Fig. 17 shows the velocity images captured using various approaches at an extremely low motion speed of 0.005 mm/s. In this case, the self-injection scheme offers a significant improvement over the conventional scheme, as shown in Fig. 17(a) and (b); the measurement errors are 0.0047 and 0.0027 mm/s, respectively. In addition, a comparison between Fig. 17(b) and (c) shows measurement errors of 0.0027 and 0.0021 mm/s, which confirms that the addition of our APD can bring further improvement. Finally, Fig. 17(c) and (d) compares the hybrid driving waveform and static laser (without FM), based on the same APD. We can see that in both cases, the quality of the velocity images is similar, as indicated by the similar measurement errors: 0.0021 and 0.0022 mm/s, respectively. The similarity in performance implies that the constant-frequency interval in the hybrid mode can independently perform motion sensing without being affected by the triangular frequency sweeps. This result indicates that our 4-D FMCW LiDAR scheme demonstrates a comparable velocity sensitivity to that of laser vibrometers, which are usually driven by a static laser under CW operation. Fig. 18 plots the normalized mean absolute error (MAE) for the measured velocities for the pixels comprising the ♡-shape obtained under different measurement conditions, as specified in this figure. The results agree with the findings illustrated in Figs. 13 to 17, that
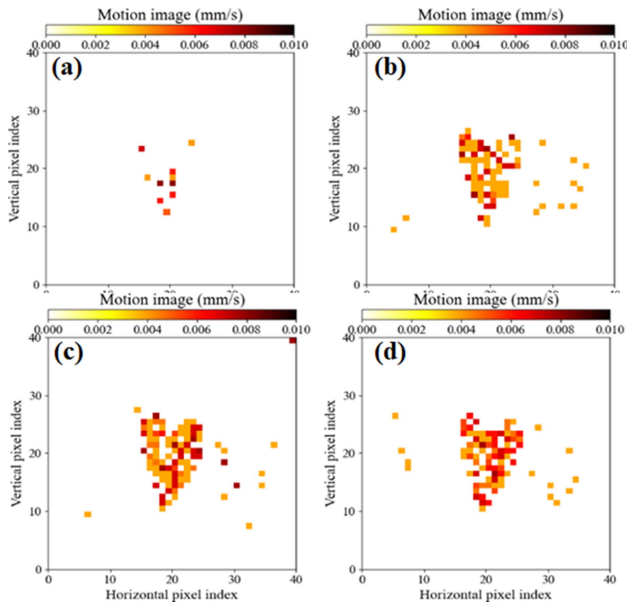
Fig. 17. Velocity images measured at 0.005 mm/sec obtained using the (a) hybrid mode with the conventional scheme and p-i-n PD, (b) hybrid mode with the self-injection scheme and p-i-n PD, (c) hybrid mode with the self-injection scheme and APD, and (d) static laser with the self-injection scheme and APD.
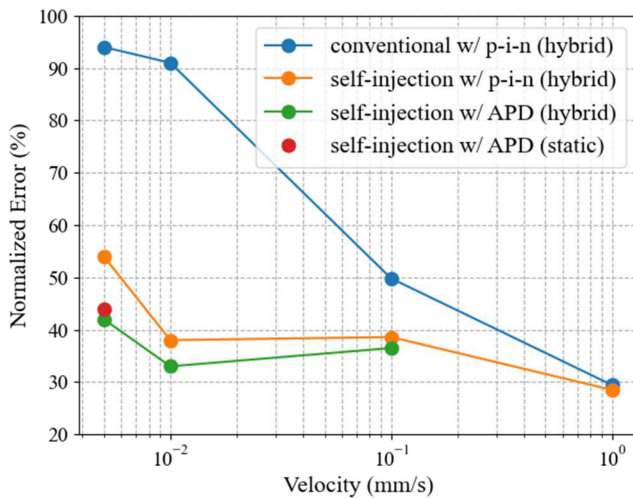

Fig. 18. Mean measurement error in velocity obtained using the hybrid FMCW and a static laser.

is, the self-injection scheme does indeed show better sensitivity, and its superiority becomes more obvious when the speed is lower. Employing the APD can further improve the low-speed motion sensing performance.

Furthermore, the velocity sensitivity demonstrated by our 4-D FMCW LiDAR system is comparable to that of a laser vibrometer with a static laser for the same system. Overall, the benefits of using a SILO include suppression of the influence of phase noise in the electrical LO signals on the down-converted baseband signal, which enhances the Doppler modulation, and provides a higher gain to amplify the IF signal, as discussed in [5]. In order to further reduce the phase noise and enhance the

quality of 4-D images, a SIL laser with an extremely narrow linewidth for wavelength sweeping on the transmitter side of LiDAR is highly desired [18], [19], [20]. To the best of our knowledge, the velocity sensitivity achieved here ($\sim 5\mu$m/sec for 4-D images) is the highest reported for the FMCW LiDAR-based technologies, including for an on-chip silicon photonic platform with a slow-light grating (75 mm/sec, 400 mm/sec [8], [11]), or for photonic crystal (19 mm/sec [29]) beam scanners and phase-diversity coherent detection (1500 mm/sec) [30].

V. CONCLUSION

A novel scheme for a 4-dimensional (D) frequency modulated continuous wave (FMCW) LiDAR is demonstrated in this work. We illustrate how the receiving end of this FMCW LiDAR can provide high-resolution 3-D + instantaneous velocity (4-D) images with an extremely high velocity sensitivity. This is achieved by combining a self-injection-locked oscillator (SILO) and high-performance avalanche photodiode (APD), which simultaneously offers high responsivity and a high saturation current, for minimizing the phase and amplitude noise, respectively. Compared to the p-i-n PD receiver, the LiDAR system with the APD can provide a much better quality of 4-D images with a higher velocity sensitivity because of the enhancement in the contrast ratio of each pixel. The velocity sensing sensitivity in our 4-D image can be further improved by driving our sweeping laser by a pre-programmed waveform to linearize the optical chirp waveform and separately measure the depth and velocity of the object in different time slots (hybrid waveform). Consequently, the SILO system produces a higher velocity sensitivity, resulting in superior 4-D images of a slow-moving ($\sim 5\mu$m/sec) object, compared to those of the reference image obtained with the conventional RF receiver. Due to improvement in the ability of the SILO-based receiving end to reduce phase noise in the down-converted baseband signals, a minor Doppler frequency shift can thus be detected with exceptional sensitivity. The reduction of phase and intensity noise in our FMCW LiDAR system opens new possibilities for the design of the next generation of 4-D LiDARs.

REFERENCES

[1] V. Winkler, "Range Doppler detection for automotive FMCW radars," in *Proc. IEEE Eur. Radar Conf.*, 2007, pp. 166–169.

[2] A. G. Stove, "Linear FMCW radar techniques," in *Proc. IEE F (Radar Signal Process.)*, 1992, vol. 139, pp. 343–350.

[3] P. Molchanov, S. Gupta, K. Kim, and K. Pulli, "Short-range FMCW monopulse radar for hand-gesture sensing," in *Proc. IEEE Radar Conf.*, 2015, pp. 1491–1496.

[4] M. Alizadeh, G. Shaker, J. C. M. D. Almeida, P. P. Morita, and S. Safavi-Naeini, "Remote monitoring of human vital signs using mm-wave FMCW radar," *IEEE Access*, vol. 7, pp. 54958–54968, 2019.

[5] W.-C. Su, M.-C. Tang, R. E. Arif, T.-S. Horng, and F.-K. Wang, "Stepped-frequency continuous-wave radar with self-injection-locking technology for monitoring multiple human vital signs," *IEEE Trans. Microw. Theory Techn.*, vol. 67, no. 12, pp. 5396–5405, Dec. 2019.

[6] F.-K. Wang et al., "Review of self-injection-locked radar systems for noncontact detection of vital signs," *IEEE J. Electromagn., RF Microw. Med. Biol.*, vol. 4, no. 4, pp. 294–307, Dec. 2020.

[7] S. Crouch, "Velocity measurement in automotive sensing: How FMCW radar and LiDAR can work together," *IEEE Potentials*, vol. 39, no. 1, pp. 15–18, Jan./Feb. 2020.

[8] T. Baba et al., "Silicon photonics FMCW LiDAR chip with a slow-light grating beam scanner," *IEEE J. Sel. Topics Quantum Electron.*, vol. 28, no. 5, Sep./Oct. 2022, Art. no. 8300208.

[9] A. Martin et al., "Photonic integrated circuit-based FMCW coherent LiDAR," *J. Lightw. Technol.*, vol. 36, no. 19, pp. 4640–4645, Oct. 2018.

[10] J.-D. Chen, K.-W. Wu, H.-L. Ho, C.-T. Lee, and F.-Y. Lin, "3-D multi-input–multi-output (MIMO) pulsed chaos LiDAR based on time-division multiplexing," *IEEE J. Sel. Topics Quantum Electron.*, vol. 28, no. 5, Sep./Oct. 2022, Art. no. 0600209.

[11] C. V. Poultan et al., "Coherent solid-state LiDAR with silicon photonic optical phased arrays," *Opt. Lett.*, vol. 42, no. 20, pp. 4091–4094, Oct. 2017.

[12] X. Zhang et al., "A large-scale microelectromechanical-systems-based silicon photonics LiDAR," *Nature*, vol. 603, pp. 253–258, Mar. 2022.

[13] S. A. Miller et al., "Large-scale optical phased array using a low-power multi-pass silicon photonic platform," *Optica*, vol. 7, no. 1, pp. 3–6, Jan. 2020.

[14] "First commercially available chip integrated FMCW LiDAR sensor," [Online]. Available: https://www.silc.com

[15] "CLV-2534 compact laser vibrometer," [Online]. Available: //hysen.com/wpcontent/uploads/2020/05/OM_DS_CLV-2534_E.pdf

[16] J. Kim and H. Sohn, "Dynamic displacement estimation by fusing LDV and LiDAR measurements via smoothing based Kalman filtering," *Mech. Syst. Signal Process.*, vol. 82, no. 1, pp. 339–355, Jan. 2017.

[17] A. G. Stove and M. B. Williams, "FMCW radar linearizer," U.S. Patent 5189427, Feb. 23, 1993.

[18] W. Jin et al., "Hertz-linewidth semiconductor lasers using CMOS-ready ultra-high-Q microresonators," *Nature Photon.*, vol. 15, pp. 346–353, May 2021.

[19] W. Liang, V. S. Ilchenko, A. A. Savchenkov, A. B. Matsko, D. Seidel, and L. Maleki, "Whispering-gallery-mode-resonator-based ultranarrow linewidth external-cavity semiconductor laser," *Opt. Lett.*, vol. 35, no. 16, pp. 2822–2824, Aug. 2010.

[20] E. Dale et al., "Ultra-narrow line tunable semiconductor lasers for coherent LiDAR applications," in *Proc. Imag. Appl. Opt.*, 2014, pp. JTu2C–JTu23.

[21] Z. Ahmad et al., "Avalanche photodiodes with multiple multiplication layers for coherent detection," *Sci. Rep.*, vol. 12, Oct. 2022, Art. no. 16541.

[22] Z. Ahmad et al., "Enhanced velocity sensitivity in 4-D FMCW LiDAR by use of avalanche photodiode with cascaded multiplication layer," in *Proc. Opt. Fiber Commun. Conf.*, 2023, Paper M3F.2.

[23] C.-H. Tseng and Y.-H. Lin, "24-GHz self-injection-locked vital-sign radar sensor with CMOS injection-locked frequency divider based on push–Push oscillator topology," *IEEE Microw. Wireless Compon. Lett.*, vol. 28, no. 11, pp. 1053–1055, Nov. 2018.

[24] C30662EH-1-InGaAs APD, 200um, TO-18, [Online]. Available: https://www.excelitas.com/product/c30662eh-1-ingaas-apd-200um-18

[25] "Photodetectors for LiDAR," [Online]. Available: https://www.hamamatsu.com/content/dam/hamamatsu-photonics/sites/documents/99_SALES_LIBRARY/ssd/Photodetector_LiDAR_kapd0005e.pdf

[26] S. Lee et al., "High gain, low noise 1550 nm GaAsSb/AlGaAsSb avalanche photodiodes," *Optica*, vol. 10, no. 2, pp. 147–154, Feb. 2023.

[27] S. Gao, M. O. Sullivan, and R. Hui, "Complex-optical-field LiDAR system for range and vector velocity measurement," *Opt. Exp.*, vol. 20, no. 23, pp. 25867–25875, Nov. 2012.

[28] X. Zhang, J. Pouls, and M. C. Wu, "Laser frequency sweep linearization by iterative learning pre-distortion for FMCW LiDAR," *Opt. Exp.*, vol. 27, no. 7, pp. 9965–9974, Apr. 2019.

[29] S. Suyama, H. Ito, R. Kurahashi, H. Abe, and T. Baba, "Doppler velocimeter and vibrometer FMCW LiDAR with Si photonic crystal beam scanner," *Opt. Exp.*, vol. 29, no. 19, pp. 30727–30734, Sep. 2021.

[30] Z. Xu, H. Zhang, K. Chen, D. Zhu, and S. Pan, "FMCW LiDAR using phase-diversity coherent detection to avoid signal aliasing," *IEEE Photon. Tech. Lett.*, vol. 31, no. 22, pp. 1822–1825, Nov. 2019.

Zohauddin Ahmad was born in Bihar, India, in 1989. He received the master's degree from the Department of Nanoscience and Nanotechnology, Jamia Millia Islamia, New Delhi, India, and the Ph.D. degree from the Department of Electrical Engineering, National Central University, Taoyuan City, Taiwan. His research interests include APD development for FMCW-LiDAR, photonics integrated circuits, and high-speed modulator-based lasers.

Sung-Yi Ou, biography is not available at the time of publication.

Wei-Chih Su was born in Changhua, Taiwan, in December 1990. He received the B.S.E.E. and M.S.E.E. degrees in 2013 and 2015, respectively, from National Sun Yat-Sen University, Kaohsiung, Taiwan, where he is currently working toward the Ph.D. degree in electrical engineering. His research focuses on vital sign detection using novel radar technology. Since 2018, he has been holding a Ph.D. Fellowship with National Sun Yat-sen University.

Yan-Chieh Chang was born in Taipei, Taiwan in 1998. He is working toward the master's degree from the Department of Electrical Engineering, National Central University, Taoyuan City, Taiwan. His research interests include fabrication of novel avalanche photodiode and single photon avalanche photodiode.

Naseem was born in the Punjab, India in 1991. He received the M.Tech. degree from the Department of Nanotechnology, Jamia Millia Islamia, New Delhi, India, and the Ph.D. degree from the Department of Electrical Engineering, National Central University, Taoyuan City, Taiwan. His research interests include high-speed photodiodes and avalanche photodiodes for optical receivers.

Jye-Hong Chen received the B.S. and M.S. degrees in electrical engineering from National Taiwan University, Taipei, Taiwan, in 1988 and 1990, respectively, and the Ph.D. degree in electrical engineering and computer science from the University of Maryland Baltimore County, Baltimore, MD, USA, in 1998.

In 1998, he joined JDSU as a Senior Engineer and obtained 15 U.S. patents. In 2003, he joined the Faculty of National Chiao-Tung University, Taiwan, where he is currently a Professor and Chairman of the Department of Photonics. He authored or coauthored more than 100 papers in international journals and conferences and has been invited to give talks at numerous technical conferences including OFC, Photonic West, and ECOC. His research interests include hybrid access networks, long reach passive optical networks, and optical interconnects.

Yu-Xiang Lin was born in Tainan, Taiwan in 1997. He is currently working toward the master's degree from the Department of Electrical Engineering, National Central University, Taoyuan City, Taiwan, and Department of Photonics, National Sun Yat-Sen University, Kaohsiung, Taiwan. His research interests include optical and electrical signal processing, and FMCW-LiDAR.

Yung-Jr Hung (Member, IEEE) received the B.S. and Ph.D. degree in electrical engineering from the National Taiwan University of Science and Technology, Taipei, Taiwan, in 2005 and 2010, respectively. From 2009 to 2010, he was a Visiting Scholar with the Department of Electrical and Computer Engineering, University of California at Santa Barbara, Santa Barbara, CA, USA. In 2013, he joined the Faculty of the Department of Photonics, National Sun Yat-Sen University, Kaohsiung, Taiwan, as an Assistant Professor and was promoted to Professor in 2021. He has authored or coauthored more than 200 technical journal and conference articles and held ten patents. His research interests include CMOS-compatible optoelectronic devices and photonic integrated circuits. He was the recipient of IEEE Best Young Professional Member Award in 2019 and MOST Da-You Wu Memorial Award in 2020.

You-Chia Chang was born in Taichung, Taiwan, on January 7, 1981. In 2018, he joined the Department of Photonics and Institute of Electro-Optical Engineering, National Chiao Tung University, Hsinchu, Taiwan, as an Assistant Professor. From 2016 to 2018, he was a Postdoctoral Research Scientist with the Department of Electrical Engineering, Columbia University, New York, NY, USA. His research interests include silicon photonics, metamaterials and 2D materials. In 2018, he was the recipient of Jade Mountain (Yushan) Young Scholar Award.

Chia-Chien Wei (Member, IEEE) received the Ph.D. degree in electro-optical engineering from National Chiao Tung University, Hsinchu, Taiwan, and the degree in electrical engineering from the University of Maryland, Baltimore, MD, USA, in 2008. In 2011, he joined National Sun Yat-sen University, Kaohsiung, Taiwan, where he is currently a Professor with the Department of Photonics. His research interests include optical and electrical signal processing and advanced modulation/demodulation schemes in optical access networks, optical interconnects, fiber-optic gyroscopes, and light detection and ranging systems.

Tzyy-Sheng Horng (Fellow, IEEE) was born in Taichung, Taiwan. He received the B.S.E.E. degree from National Taiwan University, Taipei, Taiwan, in 1985, and the M.S.E.E. and Ph.D. degrees from the University of California at Los Angeles, Los Angeles, CA, USA, in 1990 and 1992, respectively.

Since 1992, he has been with the Department of Electrical Engineering, National Sun Yat-Sen University, Kaohsiung, Taiwan, where he was the Director of the Telecommunication Research and Development Center from 2003 to 2008, the Director of the Institute of Communications Engineering from 2004 to 2007 and is currently a Chair Professor. He has authored or coauthored more than 250 technical publications in refereed journals and conference proceedings, mostly in IEEE publications. He holds more than 50 worldwide patents. His research interests include RF system-in-package for wireless communications and Doppler radars for biomedical sensing.

Dr. Horng was the recipient of the 1996 Young Scientist Award from the International Union of Radio Science, 1998 Industry-Education Cooperation Award from the Ministry of Education, Taiwan, 2011 Chair Professorship from the Advanced Semiconductor Engineering, Inc., 2012 Outstanding Research Award from National Sun Yat-sen University, 2015–2020 Outstanding Research Awards, 2020 Future Technology Award, and 2020 Most Influential Research Monograph Award from the Ministry of Science and Technology, Taiwan. He has served on the technical program committees of several international conferences, including IEEE Region 10 International Technical Conference, IEEE International Workshop on Electrical Design of Advanced Packaging and Systems, IEEE Radio and Wireless Symposium, IEEE International Symposium on Radio-Frequency Integration Technology, IEEE Electronic Components and Technology Conference, and Asia–Pacific Microwave Conference. He was on the Project Review Board of the Division of Engineering and Technologies at the Ministry of Science and Technology, Taiwan, for more than ten years, where he was the Convener of Communications Engineering Program from 2018 to 2020. He was the Founding Chair of the IEEE MTT-S Tainan Chapter in 2009. He was an Associate Editor for the IEEE TRANSACTIONS ON MICROWAVE THEORY AND TECHNIQUES from 2012 to 2015.

Jin-Wei Shi (Senior Member, IEEE) was born in Kaohsiung, Taiwan, on January 22, 1976. He received the B.S. degree in electrical engineering from National Taiwan University, Taipei, Taiwan, in 1998, and the Ph.D. degree from the Graduate Institute of Electro-Optical Engineering, National Taiwan University, Taipei, Taiwan, in 2002. He was a Visiting Scholar with the University of California, Santa Barbara (UCSB), CA, USA, in 2000 and 2001, respectively. During 2002–2003, he was a Postdoc with the Electronic Research & Service Organization, Industrial Technology Research Institute. In 2003, he joined the Department of Electrical Engineering, National Central University, Taoyuan, Taiwan, where he is currently a Professor. In 2011, he again joined the ECE Department of UCSB as a Visiting Scholar. He has authored or coauthored more than 160 Journal papers, 160 conference papers and hold 20 patents. His research interests include ultra-high speed/power optoelectronic devices, such as photodetectors, electro-absorption modulators, sub-millimeter wave photonic transmitters, and semiconductor lasers. He was an invited speaker at the 2002 IEEE LEOS, 2005 SPIE Optics East, 2007 Asia-Pacific Microwave Photonic conference (AP-MWP), 2008 Asia Optical Fiber Communication & Optoelectronic Exposition & Conference, 2011 Optical Fiber Communication, and 2012 IEEE Photonic Conference. He served on the technical program committees for the OFC 2009-2011, 2012 SSDM, 2012 MWP, and 2013 Asia-Pacific CLEO. In 2007, he was the recipient of the Excellent Young Researcher Award from the Association of Chinese IEEE and Da-You Wu Memorial Award in 2010. He has been an Optica fellow since 2023 and senior member of IEEE since 2012. He was also an Associate Editor for *Optics Express* in 2017.